Sixth International Symposium on Marine Propulsors
smp'19, Rome, Italy, May 2019

Experiments and CFD for DARPA Suboff Appended with Propeller E1658 Operating Near the Surface

L. Wang[1], J. E. Martin[1], P. M. Carrica[1], M. Felli[2], M. Falchi[2]

[1]IIHR-Hydroscience and Engineering, The University of Iowa, Iowa City, IA, 52242, USA
[2]CNR-INM, Institute of Marine Engineering, Via di Vallerano 139, 00128, Rome, Italy

ABSTRACT

Experimental and computational fluid dynamics (EFD and CFD) results of the appended notional submarine DARPA Suboff fitted with the E1658 propeller while operating near the free surface are presented. The flow measurements were taken in a phase-locked fashion using particle image velocimetry (PIV) with a multi-camera configuration in the Large Free Surface Cavitation Channel at INM. Single-phase level set numerical simulations with an overset approach were performed reproducing the experimental geometry and conditions for one advance coefficient at three shaft depths. The results reveal that the presence of the hull and the interaction with the free surface strongly affect the inflow and wake of the propeller, producing a higher local advance coefficient and blade loads near the surface. Strong free surface fluctuations at small shaft depth also cause instability and breakdown of the propeller tip vortices in the near field. Elliptic instability is observed before vortex breakdown. Comparison between CFD with EFD shows that CFD matches trends well, but under predicts wake fluctuations and thus displays more coherent phase-averaged vorticity. In addition, numerical diffusion results in a general under prediction of tip vortex vorticity and over prediction of decay rates.

Keywords

Propeller wake, Tip vortices, Submarine flow, Near-surface operation.

1 INTRODUCTION

Propeller wakes contain complex vortical structures which evolve from near field to far field in a complex physical fashion (Kumar and Mahesh, 2017). Vortex evolution in a propeller wake plays an important role in engineering applications due to a direct correlation to vibration, noise, and structural problems, but the mechanisms leading to instabilities in propeller wake are not fully understood (Felli et al, 2011).

Several experimental (Paik et al., 2007; Felli et al., 2008; Felli et al., 2011; Felli and Falchi, 2018) and numerical (Chase and Carrica, 2013; Muscari et al, 2013; Dubbioso et al, 2013; Kumar and Mahesh, 2017; Magionesi et al, 2018) studies have been conducted to investigate wake flow fields associated with isolated propellers under various operating conditions. When a ship sails under ballast conditions, or a submarine operates emerged, the propeller blades get close to the free surface. Under such condition, the influence of the free surface on the propeller is significant, possibly causing ventilation, propulsion performance deterioration, and vibrations (Wang et al, 2017; Paik, 2017). Studies of marine propellers operating near the free surface mainly focused on thrust loss and ventilation mechanisms, see for instance (Kozlowska and Steen, 2017; Guo et al., 2014; Califano and Steen, 2011a and 2011b; Kozowska et al., 2009). These studies have not dealt with effects of the presence of the free surface on the wake of a propeller.

In this paper an experimental and numerical study of the notional submarine DARPA Suboff appended with the E1658 propeller while operating near the free surface is presented. Work mainly focuses on the propeller wake and influence of the free surface on wake stability, and in analyzing the ability of the CFD approach to reproduce experimental observations, and on limitations.

2 EXPERIMENTS

Experiments were performed in the Large Free Surface Cavitation Channel at INM, with the Suboff model length $L_0 = 4.356$ m and hull diameter 0.508 m. E1658 is a INM-designed seven-bladed skewed propeller with a diameter of $D = 0.25$ m. The model was supported in place by a strut in lieu of the sail, as shown in Fig. 1. An extensive set of conditions were studied, with shaft depths $1 \le z/D \le 2$, upstream velocities $1 \le U \le 3$ m/s and propeller advance coefficients $0.65 \le J \le 1$. These conditions provide a range of submarine Reynolds and Froude numbers, as well as advance coefficients and depth parameters, though in this paper we concentrate on the cases with $U = 1.5$ m/s, $J = 0.82$ and $z/D = 1, 1.5, 2$.

PIV flow measurements were performed in the wake at the vertical centerplane and extending $3.25D$ downstream of the propeller with simultaneous acquisition of three side-by-side cameras 2560 × 2160 pixels each, illuminated by a 200 mJ/pulse Nd-YAG laser with repetition rate of up to 12.5 Hz. A sketch of the experimental set-up is shown in Fig. 2. The flow measurements were taken in a phase-

locked fashion with 28 frames per rotation, resolving 4 frames per blade passage.

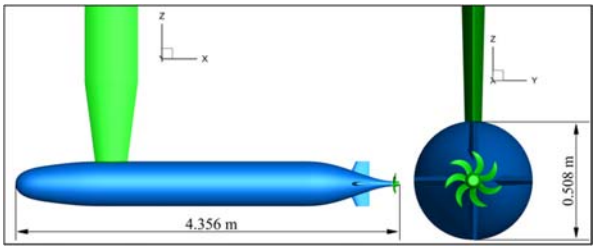

Figure 1: DARPA Suboff fitted with E1658 propeller.

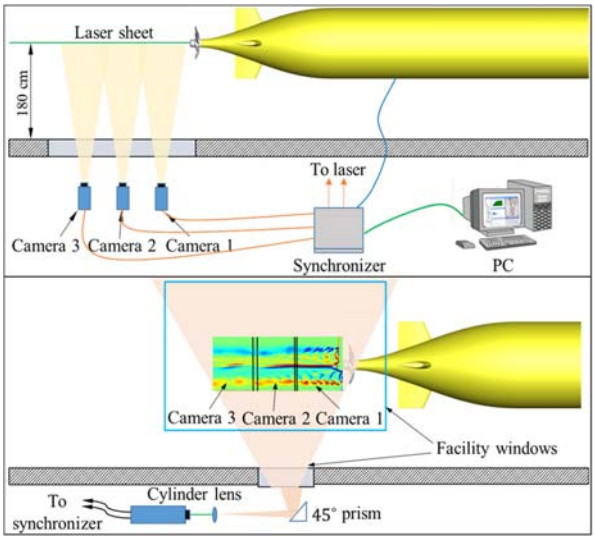

Figure 2: Top and side views of the experimental set-up.

3 CFD SIMULATIONS

3.1 REX

The code REX (Li and Carrica, 2018), developed at The University of Iowa, was used for the simulations, building on previous experience on propeller and submarine flows including Suboff and E1619 (Chase and Carrica, 2013), ONR Body-1 (Martin et al., 2015) and Joubert BB2 (Carrica et al., 2016 and 2018). REX is a general purpose CFD solver with a focus on naval hydrodynamics. A single-phase level set approach is employed to simulate the free surface (Carrica et al., 2007a) while motions are enabled by a dynamic overset technique that allows large-amplitude body motions and moving surfaces (Carrica et al. 2007b). In this paper the DDES turbulence model based on Menter's SST $k-\omega$ model is used (Menter, 1994). The convection, diffusion and temporal terms in the equations are discretized with fourth order upwind biased, second order central, and second order backwards schemes, respectively.

3.2 Grid and Simulation Conditions

The calculation domain was discretized using multi-block/overset structured grids, with free surface and propeller wake refinement blocks added to better capture the free surface and the propeller wake. Fig. 3 shows the overset grid system, with a total of 70 M grid points. CFD simulations were performed reproducing the experimental geometry and conditions but the bottom and side walls of the channel were neglected. Mimicking the experiments, results were saved locking blade phase but with a frequency of 14 solutions per rotation. The time step was chosen so that the rotor advances 1.513 degrees per step. No upstream turbulence was imposed in the CFD simulations.

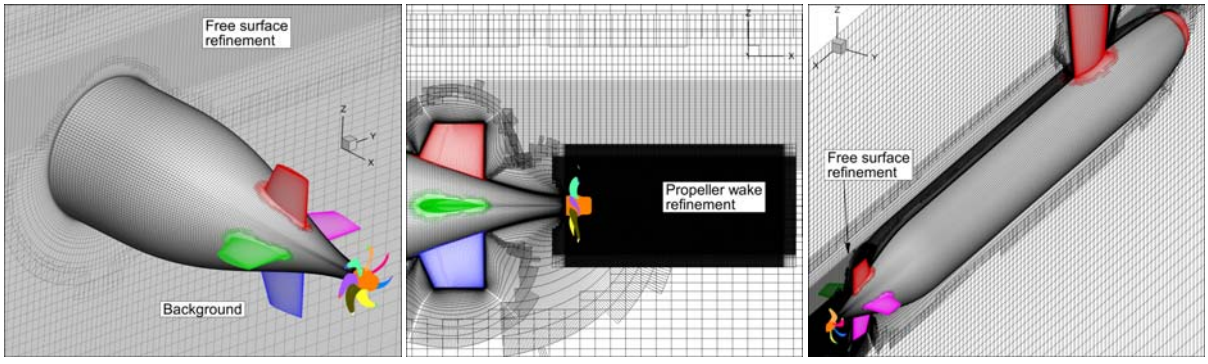

Figure 3: Overset grid system with free surface refinement and propeller wake refinement

4 RESULTS AND DISCUSSION

4.1 Instantaneous vortical structures

Fig. 4 shows instantaneous views of the simulated wake as isosurfaces of Q = 30,000 for the three shaft depths, with the vortical structures colored with non-dimensional axial velocity u/U. At the shallowest shaft depth (z/D = 1) the hull/free surface interaction is considerable, with the free surface presenting a peak about two diameters downstream of the propeller. This results in an upward transport of the propeller wake, and in a velocity defect in the hull wake that considerably destabilizes the top portion of the propeller wake. The local load on the top portion of the propeller is higher as the advance velocity is lower. This is evident observing the tip vortices in the left panel of Fig. 4, corresponding to z/D = 1. In this case the pitch between consecutive tip vortices is considerably lower at the top of the wake than at the bottom. The effect is still observable for z/D = 1.5, though the difference between top and bottom is less marked. Coloring of the tip vortices shows

that the top of the near wake for z/D = 1 experiences negative streamwise velocities.

As the shaft depth increases, the free surface-induced instability becomes weaker, and the tip vortices stay stable further downstream of the propeller. The sail wake results in additional instability on the upper side of the propeller wake, most clear at the deepest shaft position z/D = 2. The lower side of the propeller wake is considerably more stable than the upper portion, but as distance to the free surface increases the effect is less marked. Elliptic instabilities can be also observed for all depths, starting about one rotation downstream of the propeller plane and growing as the vortices break down.

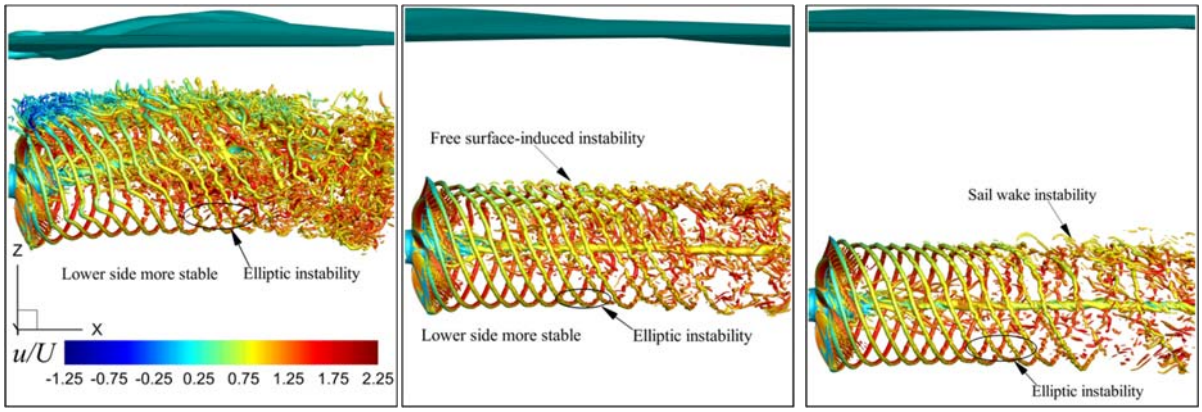

(a) J = 0.82, U = 1.5 m/s, $Z = D$ (b) J=0.82, U=1.5 m/s, $Z = 1.5D$ (c) J=0.82, U=1.5 m/s, $Z = 2D$

Figure 4: Instantaneous views of the wake of the propeller represented by isosurfaces of Q = 30000 for three shaft depths.

4.2 Phase averaged flow fields

Phase averaged quantities of out of plane vorticity ω_y, streamwise velocity u, vertical velocity w and Reynolds stresses for both CFD and EFD at the three different shaft depths are presented in Figs. 5, 6 and 7, respectively. The initial free surface is located at Z/D =0. Phase averaged quantities also support the previous description of the three-dimensional vortical structures.

For the shaft location Z/D = 1, CFD results are in good agreement with EFD, though EFD results exhibit more diffusion. This higher diffusion is caused by more wandering of tip vortices in the experiments, possibly caused by upstream water tunnel turbulence absent in the CFD simulations, and by under resolved explicit turbulent fluctuations coming from upstream in CFD. As a result, the phase averaged vorticity ω_y in Fig. 5 shows a more stable tip vortex for the lower wake in CFD, extending to $x/D \sim$ 1.2 before vortex wandering diffuse the vorticity average. In EFD the motions start earlier, at $x/D \sim 0.75$, but the average vorticity remains higher for x/D >1.5. Vortex motions in the top of the wake mask the tip vortices, with excellent agreement between CFD and EFD.

The streamwise and vertical velocity components are also well captured by CFD, with the already discussed higher diffusion in the lower wake for the EFD results. The vertical velocity is dominated by the upward tilt of the wake, which masks the hub vortex swirl evident at other shafts depth discussed later. Phase-locked Reynolds stresses, shown in the bottom panels of Fig. 5, are very high in the upper wake close to the free surface, as significant velocity fluctuations occur in a point in space in that region due to motions of the free surface and instabilities in the propeller wake. As expected, the shear stress $\langle u'w' \rangle$ is positive at the top where an increase in vertical velocity lifts the wake and results in a higher streamwise velocity. Drifting and instabilities in the highly energetic hub vortex cause very large Reynolds stresses in its path, in particular in $\langle w'w' \rangle$ which is most sensitive to small sideways motions of the vortex. In general, the agreement of CFD with EFD is very good for this depth condition where the free surface is very close to the propeller.

For the case with the shaft at higher depths Z/D = 1.5 and 2, shown respectively in Figs. 6 and 7, the influence of the free surface on the propeller wake is considerably weaker. The propeller wake tends to be more stable as the depth increases, with the top and bottom of the propeller wake looking more similar. The phase averaged vorticity ω_y still shows evidence of a more stable lower wake at Z/D = 1.5 and to a less extent at Z/D = 2, especially in CFD, though differences between upper and lower wake tend to decrease. At these higher depths the decreased effect of free surface fluctuations and hull/free surface interaction effects makes more evident the diffusion in the propeller wake not captured by CFD. Note that the sail produces additional turbulence and a horseshoe vortex that affects the upper wake of Suboff, resulting in less uniform propeller inflow than in the lower wake (Chase and Carrica, 2013). The mean streamwise velocity is less affected by drifting tip vortices and wake, and therefore agrees better between CFD and EFD. However, the trailing edge velocity deficit is clearly noticeable for CFD, particularly for Z/D = 2, but is barely present in EFD.

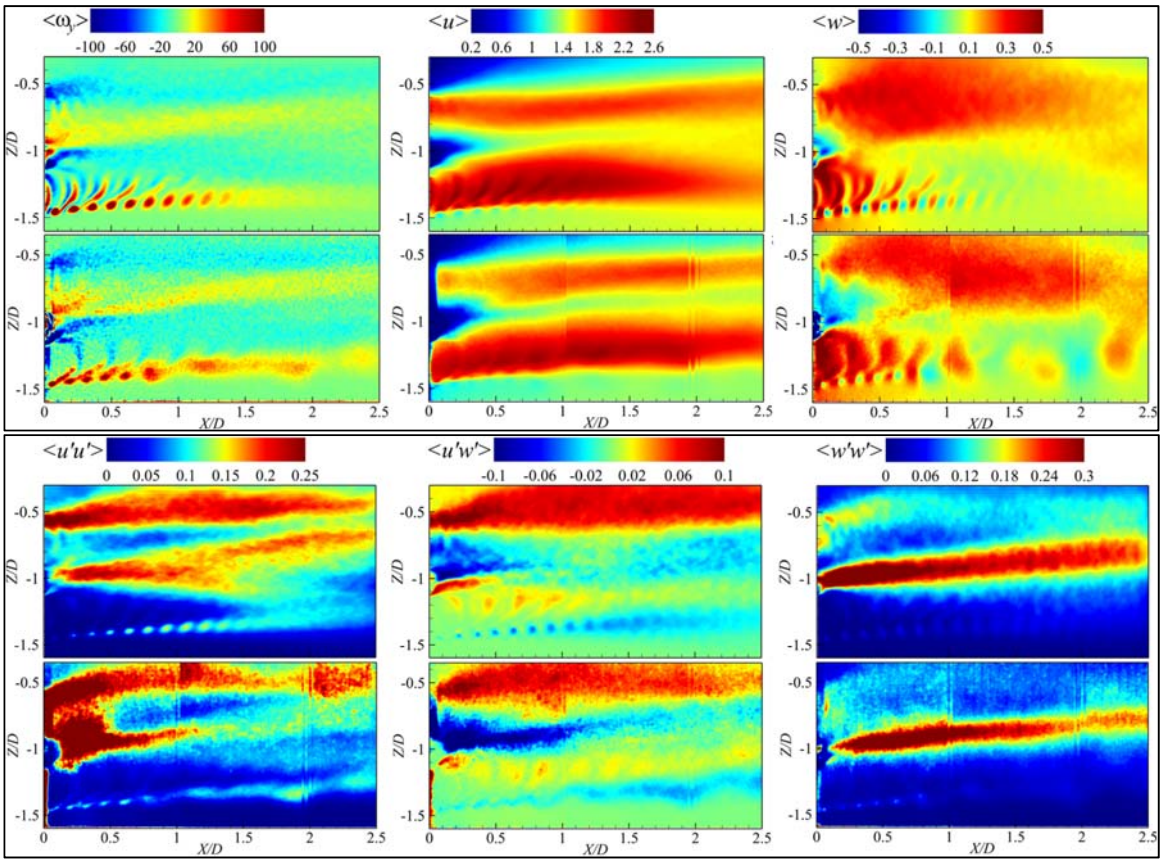

Figure 5: Phase averaged flow quantities for $J = 0.82$, $U = 1.5$ m/s, $Z = D$. Each panel top: CFD, bottom: EFD.

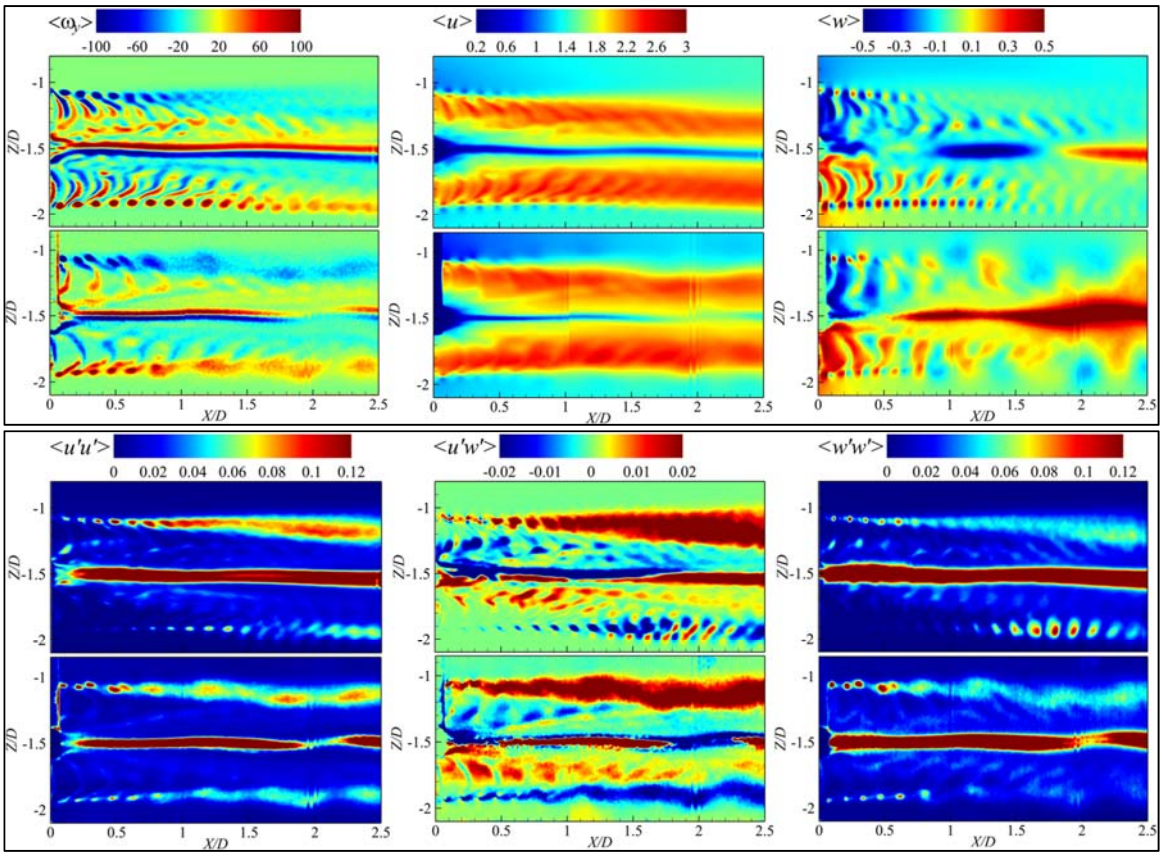

Figure 6: Phase averaged flow quantities for $J = 0.82$, $U = 1.5$ m/s, $Z = 1.5D$. Each panel top: CFD, bottom: EFD.

The vertical velocity at higher depths is highly sensitive to drifting of the propeller wake/hub vortex, as well as to the position of the PIV plane in experiments. A perfectly symmetric propeller wake would exhibit an average vertical velocity around zero with small fluctuations due to azimuthal vortices and radial flow, but Figs. 6 and 7 show that the vertical velocity in EFD is mostly positive, indicating either a drift of the wake to starboard or a wake drift caused by a slight starboard shift of the suboff model in the experiment. CFD, which cross-section in Figs. 5, 6 and 7 is located exactly at y=0 and is perfectly symmetric, exhibits some drifting of the hub vortex that causes the vertical velocity to shift from positive to negative and back to positive as the wake ages. The Reynolds stresses decrease considerably with depth, but still remain higher for the upper propeller wake than for the lower section. Fluctuations around the hub vortex present the largest Reynolds stresses. Notice that at Z/D = 2 the Reynolds stresses are slightly higher in EFD than CFD, but not very different except for $\langle u'u' \rangle$.

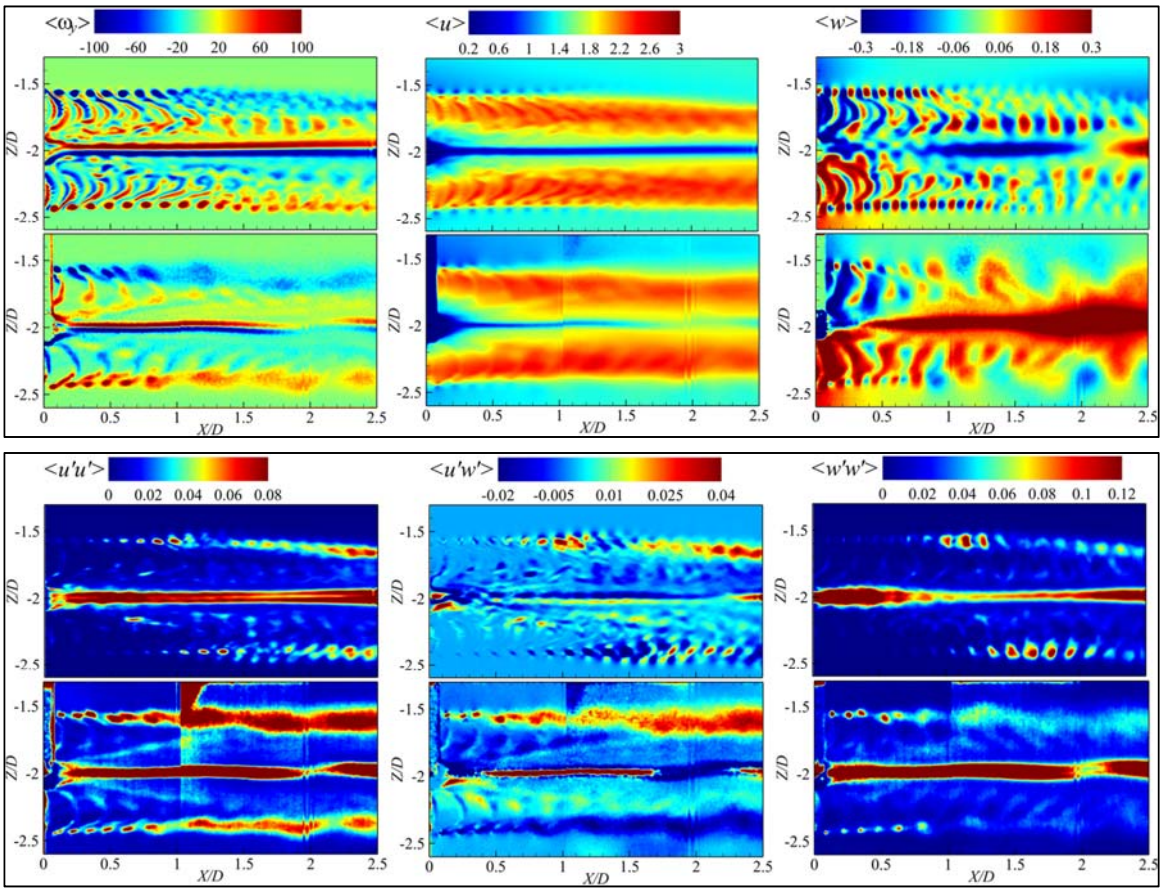

Figure 7: Phase averaged flow quantities for J = 0.82, U = 1.5 m/s, Z = 2D. Each panel top: CFD, bottom: EFD.

4.3 Instantaneous vorticity decay

As shown in the previous section, the comparison of averaged quantities between EFD and CFD can be affected by vortex wandering which makes difficult to distinguish between physical dispersion and diffusion, numerical diffusion and averaging artifacts. By comparing the instantaneous vorticity, the drifting of the vortices due to large-scale turbulence or, in the case of free surface flows, by fluctuations in free surface elevation can be eliminated. Numerical diffusion affecting the decay of vorticity can thus be quantified, indicating the quality of the CFD approach for a highly complex flow like the propeller wake.

Figure 8 shows snapshots of the CFD and EFD vorticity fields at three depths. While qualitatively the flow fields look similar, there are important differences to note. At all depths the tip vortex paths are more organized in CFD, with EFD showing earlier instability. This is particularly clear at Z/D = 2 where the free surface effects are less important. There are several possible reasons for this behavior; we speculate that upstream unresolved turbulence from the hull boundary layer and flow around sail and stern planes, as well as free stream turbulence levels in the experiment might cause vortex instability that results in earlier breakdown in EFD. On the upper vortices near the surface EFD shows early breakdown not well captured by CFD. In addition, the vortex cores are smaller in EFD, indicating lower vorticity dissipation and that the CFD grid may need further refinement.

In order to further investigate behavior of the upper side positive and lower side negative tip vortices, we record the maximum vorticity of the propeller wake inside a series of selected boxes at all phase-locked time steps or images for both EFD and CFD results. Figure 9 shows an example sketch of selected boxes and the out of plane vorticity field for CFD, where the size of the boxes guarantees that one and only one tip vortex will be located inside the box for all measured images or simulated time steps. In EFD is more difficult to guarantee that only one vortex will be present inside the box, since there is considerable additional wandering of the tip vortices and, for the closest distance to the surface, tip vortices are indistinguishable at some time snapshots. Figure 10 shows the distribution of maximum vorticity inside a selected box for all phase-locked EFD snapshots. The average maximum vorticity $\omega_{max,av}$ of all time steps and average maximum vorticity plus one standard deviation $\omega_{max,av}+\sigma$ are marked in the figure, indicating a measure of the typical and maximum tip vortex strength attributable to a location.

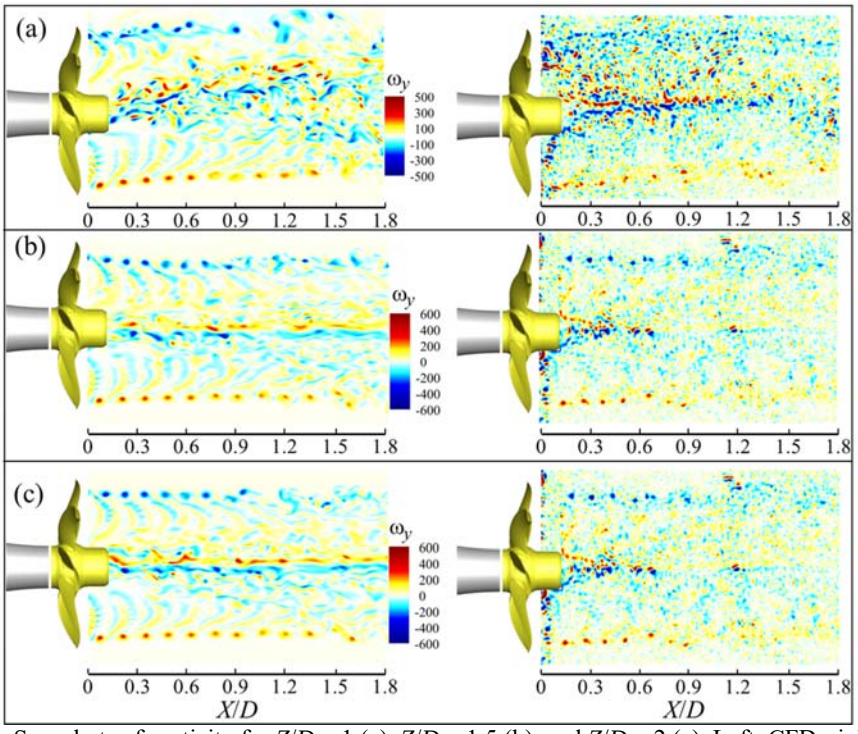

Figure 8: Snapshots of vorticity for $Z/D = 1$ (a), $Z/D = 1.5$ (b), and $Z/D = 2$ (c). Left: CFD, right: EFD.

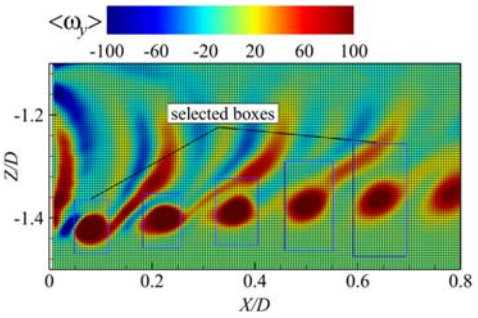

Figure 9: Sketch of downstream selected boxes.

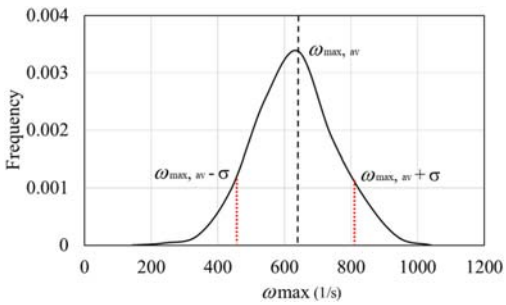

Figure 10: Maximum vorticity distribution.

Figures 11, 12 and 13 show $\omega_{max,\,av}$ and $\omega_{max,\,av}+\sigma$ as a function of the distance to the propeller for the three shaft depth conditions. Both tip vortices on the upper propeller wake (negative out of plane vorticity ω_y) and on the lower wake (positive vorticity) are shown and discussed. Measured vorticity is consistently higher than CFD predictions for all shaft depths and for both the lower and upper tip vortices. When using $\omega_{max,\,av}+\sigma$ as metric the difference is even higher, in particular for the upper vortex in the cases with the shaft closer to the surface, where maximum EFD vorticity can be twice the CFD vorticity. Differences are smaller for the lower tip vortices, less subject to the effects of free surface and of the sail wake.

The higher load on the upper tip vortices is reflected by higher vorticity, most notable in EFD but also present in CFD. This higher load, resulting from the lower propeller inflow velocity in the wake of the sail and presence of the free surface, is accompanied by higher turbulence levels that are unresolved in CFD. Notice that vortices with strength $\omega_{max,\,av}+\sigma$ are much stronger than those with

strength $\omega_{max,\,av}$, while in CFD the differences are much smaller. This indicates a large range of blade loads for EFD, not well captured by CFD. To better match the experiments a direct resolved LES or a hybrid RANS/LES method explicitly imposing synthetic turbulence mimicking the channel turbulence as well as the boundary layer turbulence may be needed, see for instance Li et al. (2018).

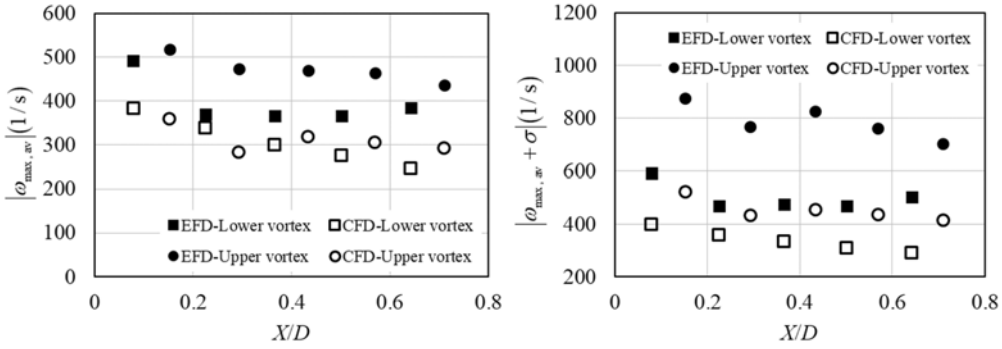

Figure 11: Tip vortex strength (computed as $\omega_{max,\,av}$ and $\omega_{max,\,av}+\sigma$) for $J = 0.82$, $U = 1.5$ m/s, $Z = D$.

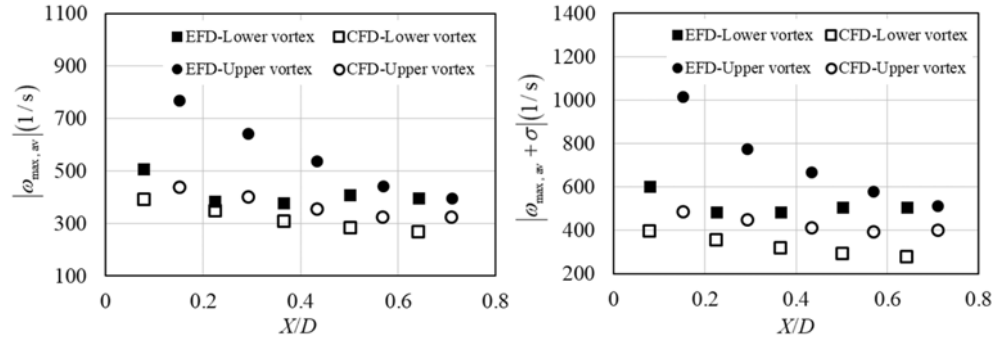

Figure 12: Tip vortex strength (computed as $\omega_{max,\,av}$ and $\omega_{max,\,av}+\sigma$) for $J = 0.82$, $U = 1.5$ m/s, $Z = 1.5D$.

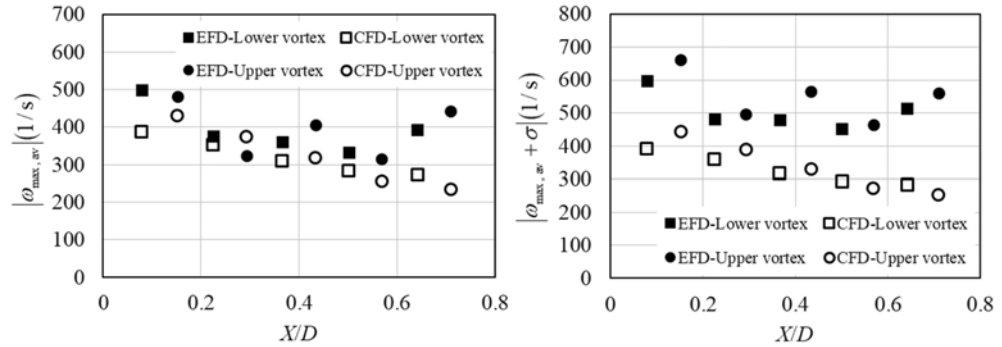

Figure 13: Tip vortex strength (computed as $\omega_{max,\,av}$ and $\omega_{max,\,av}+\sigma$) for $J = 0.82$, $U = 1.5$ m/s, $Z = 2D$.

4.4 Thrust and torque

Operation near the surface results in propeller inflow changes, including higher turbulence levels and less uniform average flow field. Thrust and torque coefficients decrease with depth as the average advance velocity and advance coefficient increase, see Fig. 14. This effect comes accompanied by considerable higher fluctuations when operating near the surface, as shown in Fig. 15. At Z/D = 2 the KT and KQ exhibit fluctuations caused mostly by the response to the wake of Suboff, dominated by the wake of the sail and stern planes. At the shallowest depth Z/D = 1 KT exhibits peak-to-peak variations of over 30% of the mean, dominated by low-frequency fluctuations with periods around 0.5 to 1 s. Free surface effects on thrust and torque fluctuations decay quickly with depth: at Z/D = 1.5 the large fluctuations due to turbulence are considerably milder than at Z/D = 1 and closer to results at Z/D = 2. Thrust and torque time variations of smaller amplitude and longer period are present at all depths, most clearly at Z/D = 2, and are due to free surface elevation fluctuations.

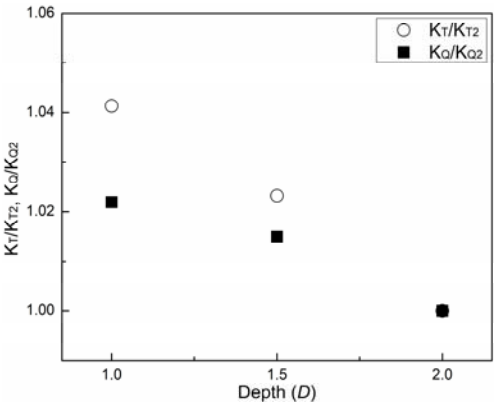

Figure 14: Thrust and torque coefficients.

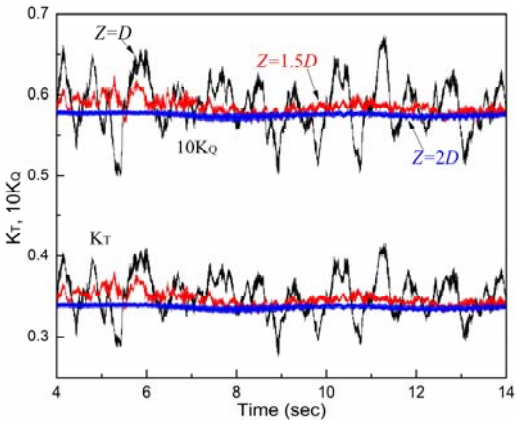

Figure 15: Time histories of thrust and torque coefficients.

5 CONCLUSIONS

Experiments based on PIV measurements and numerical simulations using the DDES solver REX are performed to analyze the wake characteristics of propeller E1658 operating behind the DARPA Suboff near the free surface. Three shaft depths were studied.

The results reveal that the presence of the hull and the interaction with the free surface strongly affect the inflow to the propeller, producing a much higher local advance coefficient and blade loads near the surface. Strong free surface fluctuations at shallow shaft depths also cause instability and breakdown of the propeller tip vortices in the near field. While CFD agrees fairly well with experiments when comparing phase-averaged quantities, instantaneous flow fields show that CFD underpredicts tip vortex strength, predicts vortex instabilities farther downstream from the propeller plane, and lacks explicit turbulent velocity fluctuations incoming into the propeller, except for those caused by the free surface.

Future and ongoing work concentrates on further studying tip vortex decay and instabilities, as well as on imposing explicit turbulent velocity fluctuations with a hybrid RANS/LES approach.

6 ACKNOWLEDGEMENTS

This research was sponsored by the US Office of Naval Reseach under grant N00014-17-1-2293, Dr. Ki-Han Kim program officer, and grant N62909-15-1-2007, Drs K.-H. Kim (ONR HQs), A. Salahuddin (ONR Global) and W.-M. Lin (formerly ONR Global) program officers. Computations were performed at the DoD HPCMP system Centennial.

REFERENCES

Califano, A., & Steen, S. (2011a). 'Numerical simulations of a fully submerged propeller subject to ventilation'. Ocean engineering, 38(14-15), 1582-1599.

Califano, A., & Steen, S. (2011b). 'Identification of ventilation regimes of a marine propeller by means of dynamic-loads analysis'. Ocean Engineering, 38(14-15), 1600-1610.

Carrica, P. M., Wilson, R. V., & Stern, F. (2007a). 'An unsteady single-phase level set method for viscous free surface flows'. International Journal for Numerical Methods in Fluids, 53(2), 229-256.

Carrica, P. M., Wilson, R. V., Noack, R., & Stern, F. (2007b). 'Ship motions using single-phase level set with dynamic overset grids'. Computers and Fluids, 36, 1415-1433.

Carrica, P. M., Kerkvliet, M., Quadvlieg, F., Pontarelli, M., & Martin, J. E. (2016). 'CFD simulations and experiments of a maneuvering generic submarine and prognosis for simulation of near surface operation'. 31st Symposium on Naval Hydrodynamics, Monterey, California.

Carrica, P. M., Kim, Y., & Martin, J. E. (2018). 'Near surface operation of a generic submarine in calm water and waves'. 32nd Symposium on Naval Hydrodynamics, Hamburg, Germany.

Chase, N., & Carrica, P. M. (2013). 'CFD simulations of a submarine propeller and application to self-propulsion of a submarine'. Ocean Engineering, 60, 68-80.

Dubbioso, G., Muscari, R., & Di Mascio, A. (2013). 'Analysis of the performance of a marine propeller operating in oblique flow'. Computers & Fluids, 75, 86-102.

Felli, M., Guj, G., & Camussi, R. (2008). 'Effect of the number of blades on propeller wake evolution'. Experiments in Fluids, 44.3, 409-418.

Felli, M., Camussi, R., & Di Felice, F. (2011). 'Mechanisms of evolution of the propeller wake in the transition and far fields'. Journal of Fluid Mechanics, 682, 5-53.

Felli, M., & Falchi, M. (2018). 'Propeller wake evolution mechanisms in oblique flow conditions'. Journal of Fluid Mechanics, 845, 520-559.

Guo, C. Y., Zhao, D. G., & Sun, Y. (2014). 'Numerical simulation and experimental research on hydrodynamic performance of propeller with varying shaft depths'. China Ocean Engineering, 28(2), 271-282.

Kozlowska, A. M., Steen, S., & Koushan, K. (2009). 'Classification of different type of propeller ventilation and ventilation inception mechanism'. First International Symposium on Marine Propulsors, Trondheim, Norway.

Kozlowska, A. M., & Steen, S. (2017). 'Experimental analysis on the risk of vortex ventilation and the free surface ventilation of marine propellers'. Applied Ocean Research, 67, 201-212.

Kumar, P., & Mahesh, K. (2017). 'Large eddy simulation of propeller wake instabilities'. Journal Fluid Mechanics, 814, 361-396.

Li, J., & Carrica P. M. (2018). 'An approach to couple velocity/pressure/void fraction in two-phase flows with incompressible liquid and compressible bubbles'. International Journal of Multiphase Flow, 102, 77-94.

Li, J., Yuan, B., & Carrica, P. M., (2018). 'Modeling bubble entrainment and transport for ship wakes: progress using hybrid RANS/LES methods'. 32nd Symposium on Naval Hydrodynamics, Hamburg, Germany.

Magionesi, F., Dubbioso, G., Muscari, R., & Di Mascio, A. (2018). 'Modal analysis of the wake past a marine propeller'. Journal of Fluid Mechanics, 855, 469-502.

Martin, J. E., Michael, T., & Carrica, P. M. (2015). 'Submarine maneuvers using direct overset simulation of appendages and propeller and coupled CFD/potential flow propeller solver'. Journal of Ship Research, 59 (1), 31-48.

Menter, F. R. (1994). 'Two-equation eddy-viscosity turbulence models for engineering applications'. AIAA Journal, 32(8), 1598-1605.

Muscari, R., Di Mascio, A., & Verzicco, R. (2013). 'Modeling of vortex dynamics in the wake of a marine propeller'. Computers and Fluids, 73, 65-79.

Paik, B. G., Kim, J., Park, Y. H., Kim, K. S., & Yu, K. K. (2007). 'Analysis of wake behind a rotating propeller using PIV technique in a cavitation tunnel'. Ocean Engineering, 34(3-4), 594-604.

Paik, K. J. (2017). 'Numerical study on the hydrodynamic characteristics of a propeller operating beneath a free surface'. International Journal of Naval Architecture and Ocean Engineering, 9(6), 655-667.

Wang, L. Z., Guo, C. Y., Wan, L., & Su, Y. M. (2017). 'Numerical analysis of propeller during heave motion near a free surface'. Marine Technology Society Journal, 51(1), 40-51.